Refractory High-Entropy Alloy Coatings for High-Temperature Aerospace and Energy Applications

9 authors, including:

Satish Dixit
Plasma Technology Inc.
9 PUBLICATIONS   242 CITATIONS

SEE PROFILE

Sal b Rodriguez
Sandia National Laboratories
48 PUBLICATIONS   186 CITATIONS

SEE PROFILE

Morgan Rae Jones
University of California, Santa Barbara
32 PUBLICATIONS   266 CITATIONS

SEE PROFILE

Peter Buzby
Plasma Technology, Inc.
2 PUBLICATIONS   16 CITATIONS

SEE PROFILE

Refractory High-Entropy Alloy Coatings for High Temperature Aerospace and Energy Applications

Satish Dixit[1], Sal Rodriguez[2], Morgan R. Jones[2], Peter Buzby[1], Rashmi Dixit[3], Nicolas Argibay[2], Frank W. DelRio[2], Hannah H. Lim[2], and Darryn Fleming[2]

1. Plasma Technology Inc., Torrance, CA 90501
2. Sandia National Laboratories, Albuquerque, NM 87185
3. DRS Research, Torrance, CA 90501

ABSTRACT

Refractory high-entropy alloys (RHEAs) were first developed a decade ago for aerospace applications, with the goal of manufacturing high-strength materials having higher structural performance than high-nickel superalloys. Herein, RHEAs were investigated as protective coatings that can provide increased erosion and corrosion resistance for high-temperature components. This is a step to demonstrating their use as a viable, cost-effective solution for both aerospace and energy industry needs. Two nearly equiatomic-composition RHEAs based on HfNbTaZr and MoNbTaVW are examined. A methodology for RHEA coating composition selection, manufacturing, and characterization is presented. It is shown that HfNbTaZr is suitable for harsh environments that do not include nuclear reactor radiation, while MoNbTaVW is suitable for harsh environments that include radiation. The air plasma spray (APS) and high velocity oxygen fuel (HVOF) thermal spray coating process is used to deposit 50 to 200-µm thick functional coatings on stainless steel (SS) 321 and Inconel 718 substrates. Contact force-dependent friction and wear rates, as well as depth- and strain rate-dependent hardness, were obtained using spheroconical scratch-based and nanoindentation methods. The data show excellent adhesive properties, high strength, and reasonable homogeneity.

1   INTRODUCTION

New materials are needed that can survive higher operating temperatures in energy applications, such as gas turbines for power generation, where thermal efficiency is limited by the operating temperature. Alloys for these applications must be resistant to erosion, corrosion, wear, and creep. Currently, component failures under such harsh environments remain a key challenge, including applications such as the supercritical carbon dioxide (sCO_2) Brayton Cycle, which has a strong potential for higher-efficiency energy production if erosion and long-term reliability issues can be overcome. High-temperature advanced nuclear reactors require materials that have high-strength at elevated temperatures and are resistant to corrosion and radiation. Consequently, the development of new superalloys that can significantly extend the performance of nuclear reactors, turbines, compressors, and heat exchangers under harsh environments is a key focus area for academia, industry, and government research.

Potential benefits of RHEA coatings include wear, erosion, and abrasion resistance, as well as high-strength layers for high-temperature applications. For example, erosion resistance is desirable for systems under high-velocity flows that have impurities, as the undesired particles impinge upon the material surface, thereby potentially causing significant levels of erosion in critical system components such as diffusers and turbine blades. Consider the middle image with a red loop in Fig. 1, which shows

significant erosion in an sCO2 diffuser for a Brayton cycle as a result of the impingement of high-velocity metallic impurities. It is for those very reasons that scratch-tests were conducted herein, to demonstrate that high-temperature refractory coatings can be well-adhered and can withstand erosive and abrasive forces for high-temperature diffusers, turbine blades, etc.
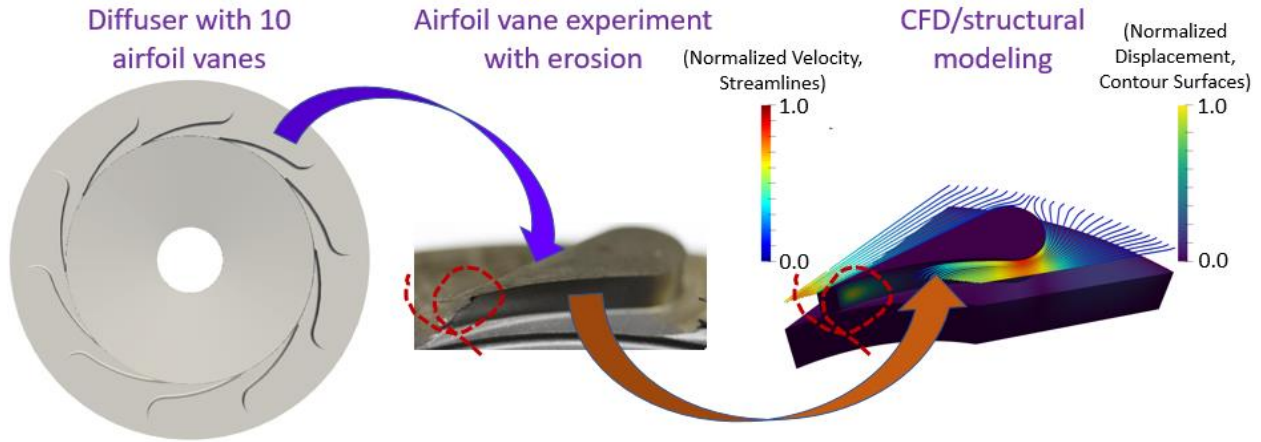

Figure 1. Erosion experimental data and modeling of an sCO₂ loop diffuser component. The region enclosed with the red dashed loop shows where erosion is prevalent [13].

First manufactured in 2010, refractory high-entropy alloys (RHEAs) were conceived for aerospace applications requiring high-strength materials with better structural performance than high-nickel superalloys [1]. Since then, much progress has been made in the field, such as the use of diverse manufacturing processes and specialized implementations (e.g., coatings and low-density alloys) [1-3]. This has resulted in myriads of potential applications for the aerospace and energy sectors [4]. However, whereas industrial applications of coatings are prevalent and well-known for their beneficial properties, such as reduced friction, wear resistance, and increased toughness, while adding a nearly-negligible layer onto high-performance components [5], the state-of-the-art development for RHEA coatings is at the initial stages, with a technology readiness level of approximately 3 to 4 [6,3,7]. Though the 11-year-old RHEA research applies to coatings, many questions remain unanswered, including coating process, particle temperature and velocity, homogeneity, and adhesion. Additional coating characteristics include hardness, porosity, and thickness.

Postprocessing temperature is typically inversely proportional to atomic diffusivity, and thereby provides a more optimal materials solution to increase homogeneity, grain size, structural strength, and corrosion- and erosion-resistance. As with the application of solid RHEA components, RHEA coatings can benefit from post processing, including annealing and polishing; certainly, more investigations are warranted [8,9].

In this work, the properties of HfNbTaZr and MoNbTaVW RHEA coatings were evaluated, including their strength, friction, wear, and erosion behavior.

2 AEROSPACE AND ENERGY APPLICATIONS

The aerospace industry seeks alloys with significantly higher yield stress than Inconel alloys, having operating temperatures up to 1,427 °C [2,600 °F]. This temperature exceeds the melting temperature of most nickel-based superalloys, which typically have negligible yield stress at temperatures above

900 °C [1,652 °F]. Furthermore, for aerospace applications it is desirable that these superalloys exhibit ductility at low temperatures, oxidation resistance, and favorable strength-to-weight ratios.

For aerospace and high-efficiency energy applications, alloys that exceed the performance of Inconel 718 would constitute a disruptive innovation, especially alloys with a combination of high ductility at room temperature (RT) and high-temperature strength. Specifically, this involves the development of alloys exhibiting yield strengths in excess of 1,250 MPa at RT and yield strength at 500 MPa or higher for temperatures in excess of 1,200 °C [2,192 °F], while retaining significant ductility [1,2].

For energy applications, a higher operating temperature implies higher power efficiency. Therefore, so long as the economics support it, it is desirable to operate in the 700 °C [800.3 °F] to 1,000 °C [1,340 °F] range in the near term, with long-term operation goals in the 1,000 °C [1,340 °F] to 1,500 °C [2,240 °F] range. Under such scenarios, RHEA coatings can provide significant near- and long-term solutions for concentrated solar power, advanced high-temperature nuclear reactors (e.g., both gas and molten salt), high-efficiency power conversion units (e.g., sCO_2 Recompression Closed Brayton Cycles), and high-temperature combustion cycles (e.g., Allam Cycles) [9-12].

Figure 1 shows an example of the significant levels of erosion that can occur in an sCO_2 diffuser in a Brayton cycle [13], as well as recent advances in coupled computational fluid dynamics and structural modeling. The streamlines indicate the normalized velocity, while the contour surface planes denote the degree of displacement. As noted via the region enclosed by the red-dashed loop, the impingement of high-velocity debris particles causes significant levels of erosion. This can result in costly shutdowns and repairs, and hence the strong motivation to find materials that are more resistant to wear and abrasion than Inconel 718 [14].

3 RHEA COATING SELECTION

A methodology was developed to down-select RHEAs based on economics and harsh-environment survivability, including erosion, corrosion, high temperature, and radiation [15]. Despite a multitude of constraints, reasonable down selections can be made to further reduce technical risk. For example, for nuclear reactors, refractory alloys can be formed from well-known, reactor-compatible refractory elements, including Cr, Hf, Mo, Nb, Re, Ta, V, and Zr; recent combinations show strong resistance to radiation, corrosion, and creep-damage [16,17]. Radiation damage to nuclear reactors is primarily from neutrons, gamma rays, beta particles, and high-energy fission fragments. For such applications, refractory elements with a low number of protons and low material density are desirable, as the aforementioned radiation particles have a lower propensity to disrupt RHEAs formed from such elements. For aerospace applications, a reasonable risk-mitigating strategy is to start, as a basis for additional refinement, with refractory-containing commercially-available superalloy Inconels. With sufficient refractory element additions, these alloys intersect compositionally with near-/equiatomic refractory high-entropy alloys. Two nearly equiatomic-composition RHEAs based on HfNbTaZr and MoNbTaVW are considered for harsh environment applications. Equiatomic compositions were selected as a way to increase configurational entropy and to promote the formation of solid solution phases, thereby increasing strength via solution strengthening [18,19].

Refractory elements and some of its alloys are noted for having excellent wear and abrasion resistance, e.g., HfNbTiZr, MoNbTaVW, and MoNbTaTiZr [3,14,18], as well as good creep resistance [20]. The following refractory elements have varying degrees of creep resistance, including Mo, Nb, Re, Ta, and W [21]. Though prone to oxidation, some RHEAs tend to form complex protective oxide layers that

can inhibit oxidation at elevated temperatures, similar to aluminum. Such refractory elements include Cr, Mo, Ta, Ti, W, and Zr [2]. However, simple oxides can also be formed, such as Cr_2O_3, MoO_3, Ta_2O, TiO_2, WO_2, WO_3, and ZrO_2 [18,22]. More complex oxides can take the form of refractory low-entropy oxides (RLEOs), such as $CrTaO_4$, which is found to reduce oxidation significantly, as the rate kinetics are reduced from quartic to parabolic [22]; most interestingly, Ti in the presence of Cr and Ta helps enable the formation of the protective oxide layer, $CrTaO_4$ [22]. In addition, RHEA oxidation can form refractory medium-entropy oxides (RMEOs), such as $CrNbVO_6$, $CrNbTiVO_2$, and Nb_2TiO_7 [18]. Therefore, some refractory alloy combinations are ideal for seals, turbomachinery, nozzles, heat exchangers, and components subject to high levels of wear, abrasion, creep, and oxidation.

Key properties of the HfNbTaZr RHEA elements are summarized in Table 1. For convenience, the table is color-coded to provide a visual queue with respect to its key properties; green is ideal, yellow-green is low-level cautionary, yellow is cautionary, and red represents a poor application. As noted, HfNbTaZr has a high yield stress that is about 2,320 MPa at RT when properly annealed. Its high yield stress is almost twice as large as Inconel 718 at RT, which is approximately 1,250 MPa. In addition, HfNbTaZr is expected to have good erosion and corrosion properties as a result of its Hf, Nb, Ta, and Zr content, with good strength at high temperature as a result of its four nearly equiatomic refractory elements; refer to Table 1. Moreover, Nb and Ta provide HfNbTaZr a higher degree of creep resistance. Interestingly, Zr gives the RHEA excellent resistance to neutron and gamma irradiation damage, whereas Hf is a nuclear poison, with utility as a neutron absorber in the nuclear industry. Hf has a large number of protons (Z number), implying a strong ability to capture neutrons and gammas. Therefore, HfNbTaZr is suitable for non-reactor, high-temperature, high-corrosion/erosion applications where neutron capture is not an issue. Hence, suitable applications include components outside of the primary reactor system that are sufficiently away from the core, such as turbomachinery, heat exchangers, seals, bearings, and pipes, as well as any harsh-non-nuclear environments where radiation is not an issue.

Table 1. Some characteristics of the refractory elements used in the HfNbTaZr and MoNbTaVW RHEAs (Note: green is ideal, yellow-green is low-level cautionary, yellow is cautionary, and red represents a poor application.)

Refractory element / resistance to C=corrosion, Cr=creep, and R=radiation; S=high-temperature strength	Low thermal neutron absorption cross-section (< 25 barns)	Atomic number Z / dose from 1 MeV gammas (MeV/g)
Vanadium (V) / R, S	Yes / 5.08	23 / 0.352
Zirconium (Zr) / C, R, S	Yes / 0.184	40 / 0.608
Niobium (Nb) / C, Cr, R, S	Yes / 1.15	41 / 0.475
Molybdenum (Mo) / C, Cr, R, S	Yes / 2.6	42 / 0.410
Hafnium (Hf) / C, S	No / 104.0	72 / 0.752
Tantalum (Ta) / C, Cr, S	Yes / 20.6	73 / 0.617
Tungsten (W) / C, Cr, S	Yes / 18.3	74 / 0.549

For convenience, Table 1 also shows key properties for the refractory elements in MoNbTaVW, showing that the alloy is relatively impervious to nuclear radiation, as compared with HfNbTaZr. In particular, Mo, Nb, Ta, V, and W have low thermal neutron absorption cross sections that range from

1.15 to 20.6 barns, where 1 barn = 10^{-28} m^2. In addition, except for Ta and W, which have a relatively high atomic or Z number of 73 and 74, respectively, the other three refractory-element Z ranges from 23 to 42. Moreover, the Monte Carlo N-Particle transport code was used to calculate the absorbed dose of the refractory elements under irradiation from 1 MeV gammas. As noted in the table, V had the lowest dose, at 0.352 MeV/g, while the element with the highest dose, Hf, had more than twice the magnitude, at 0.752 MeV/g. Again, this analysis indicates that the Hf-based RHEA is more suitable for non-radiation applications, and as expected, the MoNbTaVW is more resistant to radiation damage. Moreover, Mo, Nb, Ta, and W provide excellent corrosion resistance, while the five equiatomic refractory elements provide high strength at elevated temperature. MoNbTaVW has also shown excellent wear resistance compared with Inconel 718; recent experiments showed up to 80% less wear [14]. Finally, Mo, Nb, Ta, and W provide excellent creep resistance. W has the highest melting point of all the refractory elements, so it comes as no surprise that it increases brittleness at lower temperatures; thus, of necessity, a balance is made with respect to radiation and corrosion endurance, high-temperature strength, creep resistance, and degree of brittleness.

Note that a similar equiatomic RHEA, MoNbTaW, was investigated as a coating using direct current magnetron sputtering [8,10,11]. Because of their similar composition, the MoNbTaVW and MoNbTaW RHEA coatings are expected to have similar performance behavior and physical properties. However, MoNbTaVW is expected to have higher entropy than MoNbTaW because it is a senary RHEA, as opposed to quaternary. Further, the addition of V is expected to improve the MoNbTaVW radiation performance in nuclear environments. Finally, note that annealing of MoNbTaW coatings at intermediate temperatures (~800 °C [1,472 °F]) results in hardening of the alloy [8].

4   THERMAL SPRAY of RHEA COATINGS

The APS and HVOF thermal spray processes are versatile methods that have the ability to deposit multi component high melting point metals, ceramics, cermets, etc. The high-energy coating process dynamics result in rapid quenching of the deposition media within a short flight event, resulting in a coating system with unique properties not realized by other thermally stable processes [23]. The RHEA particles can experience temperatures approximately 2,227 °C [4,040 °F] to 2,727 °C [4,940 °F] and velocities up to 500 m/s, which result in a unique microstructure as depicted in Figs. 2 and 3. Due to the transient nature of the process and rapid quenching of the splats as they are deposited on an air-cooled substrate, the coating develops unique properties [24-26].
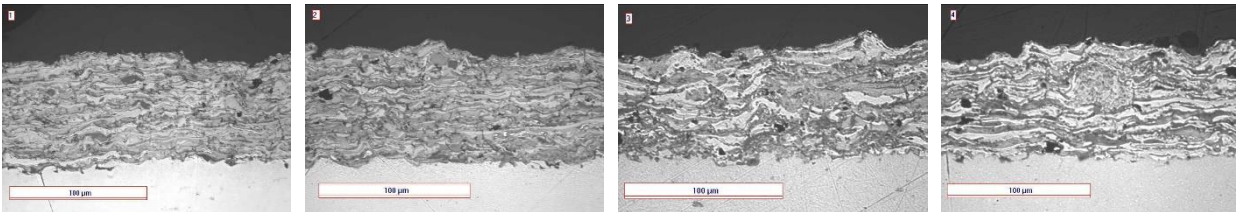

Figure 2. The HfNbTaZr and MoNbTaVW RHEA coatings using APS; bar=100 microns. (1) MoNbTaVW coating on Inconel 718 substrate, (2) MoNbTaVW coating on SS 321 substrate, (3) HfNbTaZr coating on Inconel 718 substrate, and (4) HfNbTaZr coating on SS 321 substrate.
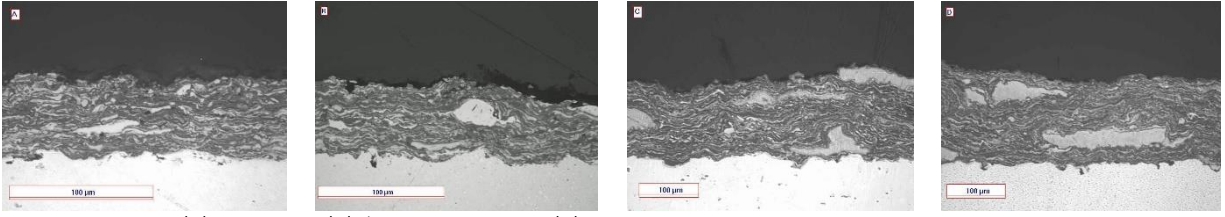
Figure 3. The HfNbTaZr and MoNbTaVW RHEA coatings using HVOF; bar=100 microns. (A) HfNbTaZr coating on Inconel 718 substrate, (B) HfNbTaZr coating on SS 321 substrate, (C) MoNbTaVW coating on Inconel 718 substrate, and (D) MoNbTaVW coating on SS 321 substrate.

Two RHEA compositions were considered for this study, MoNbTaVW and HfNbTaZr. The powders were sourced with similar particle size ranges (20-50 μm) whereby the individual metallic powders were blended in nearly equiatomic percentages in a rotating vee chamber for 30 to 40 minutes, before being used for the coating process. Both the APS and HVOF coat methods were employed, and are described next.

The APS process was carried out using the Metco 9MB APS gun with a Thermach powder feeder. The gun parameters used were a 550 amp arc current at 75 volts with a volumetric flow of 9 L/min (Liters/Minute) of hydrogen gas and 47 L/min of argon gas. The powder feed rate was set at 40 g/min and the coating standoff distance was maintained at 125 mm between the gun and the substrates. Inconel 718 and SS 321 substrates (size 25 mm x 76 mm and 1.5 mm thick) were used via panels. The substrates were cooled during the process with compressed air on the front and back, and the temperature was maintained around 93 °C [200 °F]. The overall coating thickness for each coating was kept within 100 to 250 μm and the overall measured coating roughness averaged 3.81 μm R_a. This is a bit rougher than anticipated and hence the coating microstructure showed a higher percentage of porosity and layered structure. Figures 2 and 3 show the coating microstructure of the APS and HVOF coatings, respectively.

The HVOF coating process involved a JetKote system with a 152 mm long nozzle. A metallization system was used to control the gas feed and gun ignition. The standoff distance between the gun nozzle tip and the substrates was maintained at 230 mm. The coating parameters used were fuel gas hydrogen at 280 L/min and oxygen at 635 L/min. The carrier gas was maintained at 28 L/min and the powder feed rate was 35 g/min. It was observed that the MoNbTaVW powder deposition was not ideal and built up only about 5 μm per pass, whereas the HfNbTaZr coating deposition was around 25 μm per pass. Certainly, more coating optimization work can be performed to improve the HVOF sprayability of the MoNbTaVW coating system. The HVOF coatings also showed higher roughness around 3.81 to 5.08 μm R_a, indicating the need to fine tune the feedstock particle size distribution, as well as the composition. In the near future, cold milled and gas atomized powder blends with well-defined powder morphology will be manufactured to reduce the overall roughness and improve the coating sprayability.

The metallurgical cross section microstructures at 200X magnification are shown in Fig. 2, starting from left to right, displaying the APS (1) MoNbTaVW coating on Inconel 718 substrate, (2) MoNbTaVW coating on SS 321 substrate, (3) HfNbTaZr coating on Inconel 718 substrate, and (4) HfNbTaZr coating on SS 321 substrate. The APS microstructure shows typical layered structure with

metal and oxide distribution within the matrix. Most metals like Hf, Zr, Mo, and V are highly reactive and tend to oxidize during the APS process. This might also lead to a harder phase within the RHEA coating matrix. This in turn is reflected in its wear properties as well. Figure 3 shows the HVOF cross section microstructures at 200X magnification, starting from left to right, displaying (A) HfNbTaZr coating on Inconel 718 substrate, (B) HfNbTaZr coating on SS 321 substrate, (C) MoNbTaVW coating on Inconel 718 substrate, and (D) MoNbTaVW coating on SS 321 substrate. Though the particle temperatures during the HVOF process are much lower than the plasma spray process, the velocity is twice as fast. This leads to certain erosive properties for the in-flight particles as they impinge on the growing coating surface, which might lead to surface erosion as the coating is building up. This is evident from the thinner coating build-up of both RHEA coatings on the two different substrates. Certainly, further optimization of the feed stock is required to tailor it to the HVOF deposition process. Interestingly, both the APS as well as HVOF microstructures (Figures 2 and 3) show brighter looking metallic inclusions within the matrix. We plan to further investigate these components within the matrix, their chemical states, and their effect on the mechanical as well as corrosion resistance properties. This analysis will be reported in the next report.

5 RHEA COATING MECHANICAL PROPERTIES

A summary of mechanical and material properties determined via scratch-based and nanoindentation methods, discussed in the subsections below, is presented in Table 2. Storage modulus and hardness were determined using nanoindentation techniques, and friction coefficient, wear coefficient, and stain rate sensitivity were determined using microscratch techniques.

Table 2. Summary of material properties for the four RHEA coatings for the present study.

Alloy	Storage Modulus (GPa)	Nano Indentation Hardness (GPa)	Friction Coeff.	Wear Coeff.	Strain Rate Sensitivity
HfNbTaZr on Inconel 718	125 ± 3	9.51 ± 0.62	$0.12 - 0.46$	5.9×10^{-4}	0.047 ± 0.004
HfNbTaZr on SS 321	132 ± 3	8.54 ± 0.34	$0.04 - 0.63$	4.5×10^{-4}	0.040 ± 0.005
MoNbTaVW on Inconel 718	235 ± 5	7.69 ± 0.29	$0.14 - 0.51$	3.7×10^{-4}	0.047 ± 0.004
MoNbTaVW on SS 321	215 ± 6	5.08 ± 0.59	$0.06 - 0.62$	3.3×10^{-4}	0.036 ± 0.002

5.1 Micro- and Macro-scale Mechanical Testing

RHEA-coated coupons were epoxy-potted and polished to an average surface roughness, $R_a \cong 1 \ \mu m$, to enable more accurate measurements of scratch track dimensions. Scratch-based measurements of friction coefficient, low/single-cycle wear rates, and hardness were determined from linearly ramped contact force experiments, from a contact force of 0-50 N, using a spheroconical diamond tip with a 200 μm radius and 120° cone angle (Rockwell type C, Brale indenter). Friction and wear were determined as a function of deformation depth, probing regimes of elastic, plastic, and elastoplastic behavior, as shown in the top-down interferometric topographical maps in Fig. 4. The width and

peak depth of the tracks were determined from the surface maps, and the combination of forces and wear track dimensions were used to calculate hardness and wear resistance.
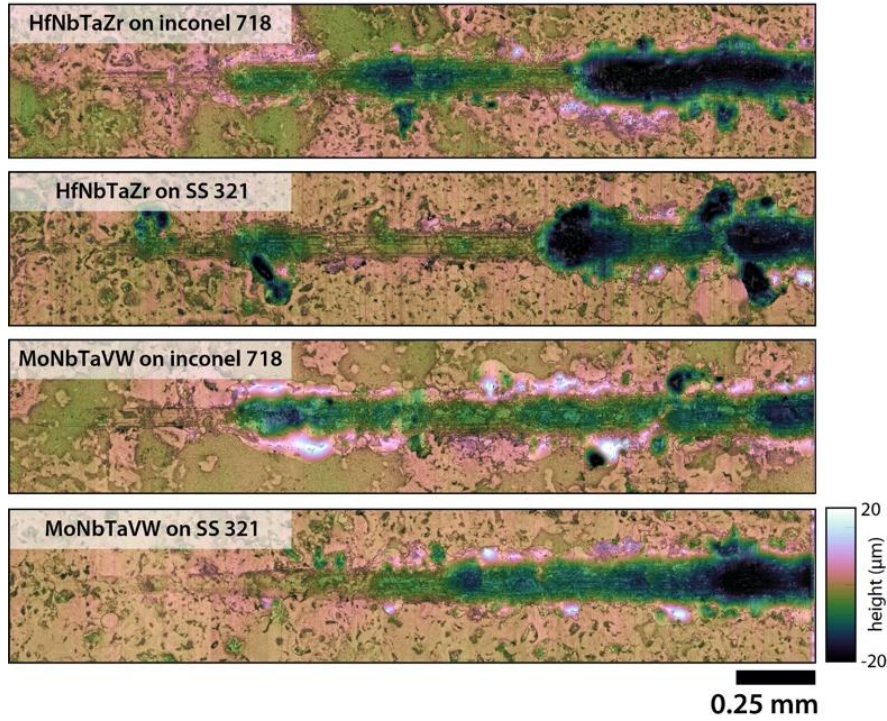

Figure 4. Interferometric topographical maps of ramped scratch experiments performed on RHEA coatings from 0 – 50 N at a ramp rate of 20 N/mm.

In one series of experiments, the tip was brought into contact and rastered against polished test coupons at a speed of 0.1 mm/s, while the applied contact force was ramped from 0 to 50 N over a length of approximately 2.5 mm. The lateral (friction) and surface-normal (contact) forces were independently measured, allowing for a calculation of the friction coefficient μ (ratio of friction and normal forces) and dimensionless Archard wear coefficient *K*, which was determined based on the ratio of cross-sectional area of material displaced by the applied force following the method described by earlier researchers [27]; results are shown in Figs. 5 and 6 for friction and wear coefficients, respectively. The modified Archard wear equation for ramped loads was used to determine the Archard wear coefficient for each RHEA coating. The average material removed along the scratch direction was determined in 0.25 mm increments, using the average penetration depth p_d and track width w to calculate the cross-sectional area loss, $A_L = p_d \cdot w$. The wear coefficient was then solved using the expression $K = \frac{A_L H}{Cx}$, where H is the average hardness value from nanoindentation, C is the ramp rate (20 N/mm), and x is the total track length.
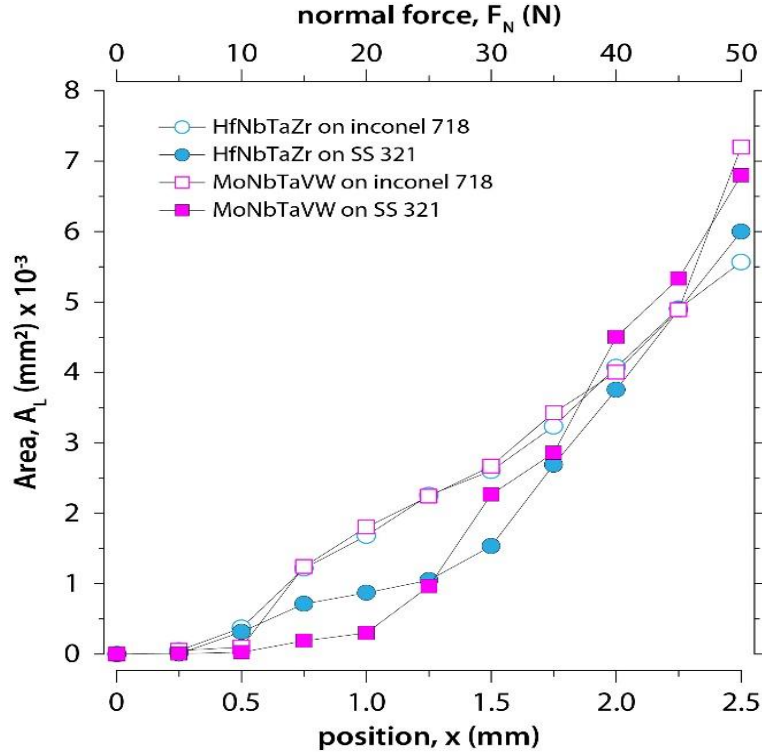
Figure 5. Area of material removal as a function of position and corresponding normal force of the four RHEA coatings.
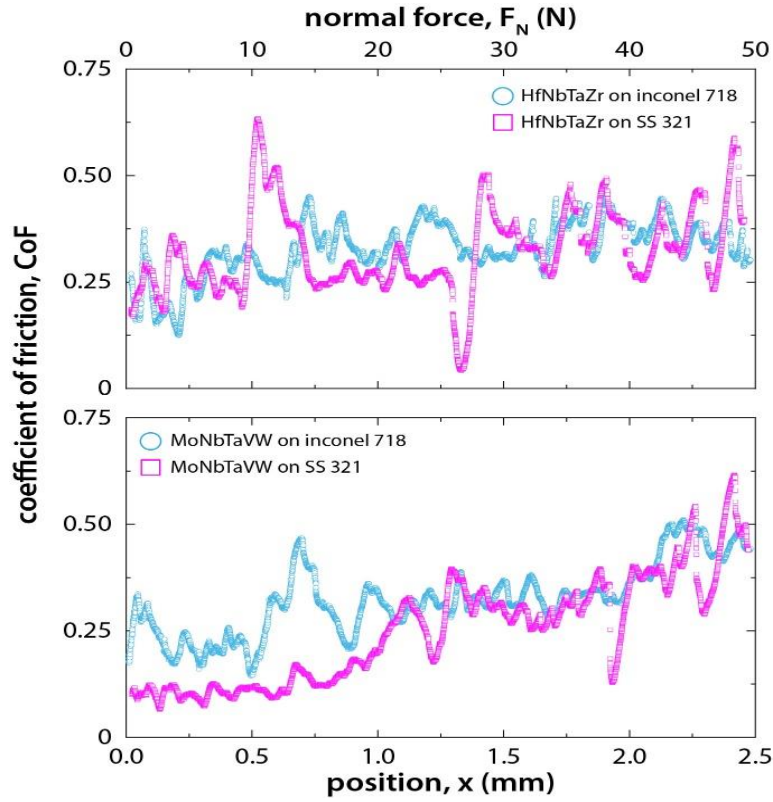

Figure 6. Coefficient of friction as a function of position and corresponding normal force for the four RHEA coatings.

Assessing the Archard wear coefficient through single pass scratch testing is a way to quantify abrasive wear in metals and metallic alloys [28-30]. Values for the four RHEA specimens are reported in Table 2. As shown in Fig. 5, past approximately 1.0 mm, the area loss of each sample assumes a linear form, suggesting a transition from predominately elastic to plastic deformation. Wear coefficients of all four samples were in the range of $K \cong 10^{-4}$, which is classified as low abrasive wear damage [28]. HfNbTaZr was determined to have higher hardness than MoNbTaVW, which has been shown to be correlated to higher wear resistance [31]. Dry sliding wear experiments on RHEAs similar in composition to MoNbTaVW showed considerable variability in reported wear coefficients; other researchers studied the wear behavior of MoNbTaTiZr, which had a wear coefficient of $K \cong 8 \times 10^{-1}$ and a hardness of $H \cong 5\,\text{GPa}$ [32], while others reported a wear coefficient of $K \cong 7 \times 10^{-4}$ [14], similar to the current values. Reciprocating, multi-cycle wear tests often lead to the formation of mixed metal-oxide layers within the wear track, which may partly explain the multiple order-of-magnitude differences in wear resistance. Additionally, differences in substrate and probe materials, normal load, and sliding speed likely contribute to differences in tribological response. Interestingly, our wear coefficients from single cycle abrasive scratch on MoNbTaVW do agree well with a multi-cycle sliding study [14]. The nanoscratch technique was also used to examine the wear resistance of HfNbTiZr [30], similar to the HfNbTaZr coating studied here. The authors determined a wear coefficient nearly two orders of magnitude higher ($K \cong 10^{-2}$), suggesting the substitution of Ti for Ta could be partly responsible for the increased wear resistance of the RHEA in the current study. Other microstructural characteristics, including the presence of intermetallic phases and differences in grain size, could contribute to differences in hardness and tribological properties.

The friction coefficients from ramped-force scratches on the RHEA coatings are shown in Fig. 6. High friction was observed across all samples, indicative of ploughing deformation. MoNbTaVW, unlike HfNbTaZr, showed force-dependent friction, and even evidence of low friction ($\mu < 0.1$) at contact forces below about 20 N. As the contact force increased, the friction coefficient of MoNbTaVW increased by ~4× on SS 321, and ~2× on Inconel 718. Previous reports have observed a similar trend in metallic glasses, which was attributed to material pile-up [27]. An increase in material pile-up can result in an increase in lateral force. Since the hardness value of MoNbTaVW is the lowest of the four samples, it is unsurprising that the sample was most susceptible to pile-up and showed the strongest dependence of friction coefficient on normal force.

Over the 2.5 mm ramped scratch track length, the average friction coefficients of HfNbTaZr on Inconel 718 and SS 321 were $\mu \cong 0.33$ and $\mu \cong 0.32$, respectively. An average friction coefficient of $\mu \cong 0.16$ was measured for equiatomic HfNbTiZr via a ramped nanoscratch technique [30]. At lower loads, the HfNbTaZr friction coefficient was lower, but gradually increased as normal load increased. Larger contact pressures via microscratch could be responsible for the higher friction coefficient (more material build up than nanoscratch). The average friction coefficients of MoNbTaVW on Inconel 718 and SS 321 were $\mu \cong 0.33$ and $\mu \cong 0.26$, respectively. A previous report on the reciprocating sliding behavior of this RHEA composition measured much higher friction coefficients ($\mu \cong 0.525 - 0.776$) [14]. The discrepancy may be a product of a combination of counter face and substrate composition, oxidation effects, and mechanical/microstructural differences.

A series of constant 50 N contact force, 4 mm long scratches were performed at sliding speeds ranging from 0.001 mm/s to 10 mm/s. Using force data, tip geometry, and high-spatial resolution interferometric surface mapping, the strain rate-dependent hardness (H) was determined [33-35]. To

summarize briefly, the strain rate $\dot{\varepsilon}$ was calculated following the convention of using the ratio of sliding speed v to scratch track peak width w, following the expression, $\dot{\varepsilon} = \frac{v}{w}$, and hardness calculated based on the ratio of contact force to projected surface-normal contact area, $H = \frac{8}{\pi}\left(\frac{F_N}{w^2}\right)$. The measured hardness of the four RHEA coatings is shown in Fig. 7, which indicate a logarithmic strain rate-dependence over five decades of strain rate. The strain rate sensitivity (m) for each coating was determined from the hardness and stain rate values using the expression $m = \frac{\partial \ln(H)}{\partial \ln(\dot{\varepsilon})}$, with results summarized in Table 2.
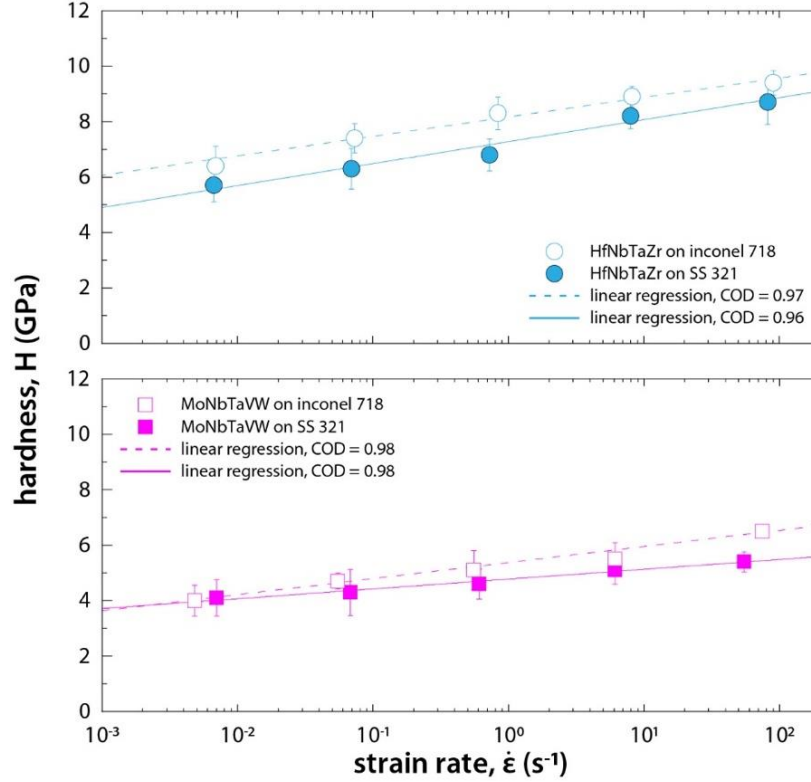

Figure 7. Strain rate dependent hardness of four RHEA coatings.

On both substrate types, HfNbTaZr hardness values were higher than MoNbTaVW across all sliding speeds. Both coatings were found to be harder on Inconel 718 than on SS 321, although coating type affected the overall hardness value more. Scratch hardness of HfNbTaZr on Inconel 718 and SS 321 ranged from $H \cong 6.1 - 9.1\ \text{GPa}$ and $H \cong 5.5 - 7.9\ \text{GPa}$, respectively. In a previous report, HfNbTaZr hardness values ranged from $H \cong 3.6\ \text{GPa}$ in the as-cast condition to $H \cong 5.6\ \text{GPa}$ after a 1 day anneal, and was attributed to elemental short-range ordering/clustering and precipitation of an intermetallic β phase [36]. Other factors can impact the hardness of RHEAs, including processing conditions, test conditions, and microstructural characteristics like grain size [37]. Specimens in the earlier work had large grains (100s of μm), which could be largely responsible for the lower hardness.

Scratch hardness of MoNbTaVW on Inconel 718 and SS 321 ranged from $H \cong 3.9 - 6.1\ \text{GPa}$ and $H \cong 4.1 - 4.8\ \text{GPa}$, respectively. Equiatomic MoNbTaVW was previously reported to have a hardness of $H \cong 5.4\ \text{GPa}$ [38], which agrees well with the current measurement.

For single-phase body-centered cubic (BCC) RHEAs, strain rate sensitivity (SRS) has been reported to be in the range of $m \cong 0.01 - 0.06$ [39]. SRS of the present RHEAs ranged from $m \cong 0.036 - 0.047$ and showed little correlation with coating or substrate composition. A recent report on the SRS of MoNbTaVW micropillars showed values in the range of $m \cong 0.016 - 0.069$, which agrees with the current findings from microscratch experiments [40]. The strain rate-dependent hardness was recently reported for HfNbTiZr, which is compositionally similar to one of the RHEAs studied here, though substituted Ta for Ti [41]. This RHEA was found to have a slightly larger strain rate sensitivity $m \cong 0.060$ using micropillar testing. The present values of SRS are comparable to those for coarse-grained BCC metals, where screw dislocation and kink-pair nucleation and motion are the dominant mechanisms for accommodation of plastic deformation [42,43].

5.2   Nanoindentation Testing

Micro/macro-scale measurements were complemented by nanoindentation measurements of hardness, using a stationary contact with ramped force and a Berkovich diamond tip (three-sided pyramid geometry). Nanoindentation was used to determine depth-dependent hardness with higher spatial resolution, thereby probing variations in strength as a function of microstructural characteristics, such as phase type and grain size.

Nanoindentation experiments were performed on a Hysitron TI-980 TriboIndenter (Bruker Nano, Minneapolis, MN) with a Berkovich tip. Prior to measurements on the polished RHEA specimens, the tip area function and load frame compliance were calibrated over the entire load range of the instrument with fused silica as the reference material. For the Berkovich tip, the tip area function was defined as $A(h_c) = C_0 h_c^2 + C_1 h_c^1 + C_2 h_c^{1/2} + C_3 h_c^{1/4} + C_4 h_c^{1/8} + C_5 h_c^{1/16}$, where h_c is contact depth and C_0 through C_5 are coefficients related to tip shape [44]. In this study, C_0 was taken to be the ideal value for a Berkovich tip ($C_0 = 24.5$), and C_1 through C_5 were found via fits to the calibration data assuming a reduced modulus $E_r = 69.6$ GPa for fused silica. The fit between the data and model validated the area function down to h_c of 30 to 40 nm. For the measurements on the polished RHEA specimens, a 3×3 array of indents was performed on each sample in load control to a maximum force of 15 mN. The indent spacing was 10 μm; this was small enough to enable multiple single-grain indents, but large enough to prevent interactions between neighboring indents [45]. For each indent, a CMX (continuous measurement of X) load function was used, which consisted of a constant strain-rate load superimposed with a 220 Hz oscillating load. The strain rate was kept constant at 0.123 s^{-1} to mitigate strain-rate effects, whereas the oscillating load was utilized to provide depth-dependent property data. From this loading scheme, the storage modulus E' was determined using $E' = k_s \sqrt{\pi}/2\sqrt{A}$, where k_s is the contact stiffness and A is the contact area. Similarly, the hardness H was assessed by $H = F_{max}/A$, where F_{max} is the maximum force and A is the contact area. E' and H were determined for RHEA films on different substrates, thereby also facilitating substrate-dependent property characterization.

Results of nanoindentation experiments performed on the four RHEA coatings are shown in Fig. 8. A total of nine nanoindents were conducted for each coating via a 3x3 array, and the average depth-dependent hardness for each coating was plotted in Fig. 8. The nine indents were averaged based on vertical displacement points, where the error bars in Fig. 8 represent the standard deviation in hardness at each point. For all specimens, past a vertical displacement of approximately 150 nm, hardness reached a steady state value, indicating a fully plastic response [46]. Therefore, the average and standard deviations storage modulus and hardness values were tabulated from 150 nm to the maximum vertical displacement, and are listed in Table 2. Nanoindentation hardness of HfNbTaZr on Inconel 718 and

SS 321 was $H \cong 9.5\,\text{GPa}$ and $H \cong 8.5\,\text{GPa}$, respectively. Storage modulus values did not differ considerably between the two substrates, HfNbTaZr on Inconel 718 having a value of $E' \cong 125\,\text{GPa}$ and HfNbTaZr on SS 321 having a value of $E' \cong 132\,\text{GPa}$. Values of storage modulus agree with previous reports [47]. Average nanoindentation hardness differed by approximately $\Delta H \cong 1\,\text{GPa}$ between substrates, similar to microscratch results. Comparing average hardness values, nanoindentation tended to skew on the higher end of values measured with microscratch techniques. Size effects could be partially responsible for this phenomenon; nanoindentation probes a small sample volume at a particular location on the sample, whereas scratch testing over a 4 mm track length represents a global average hardness of the sample. Additionally, penetration depths are orders of magnitude larger in microscratch, leaving a possibility of substrate hardness contributions to hardness.
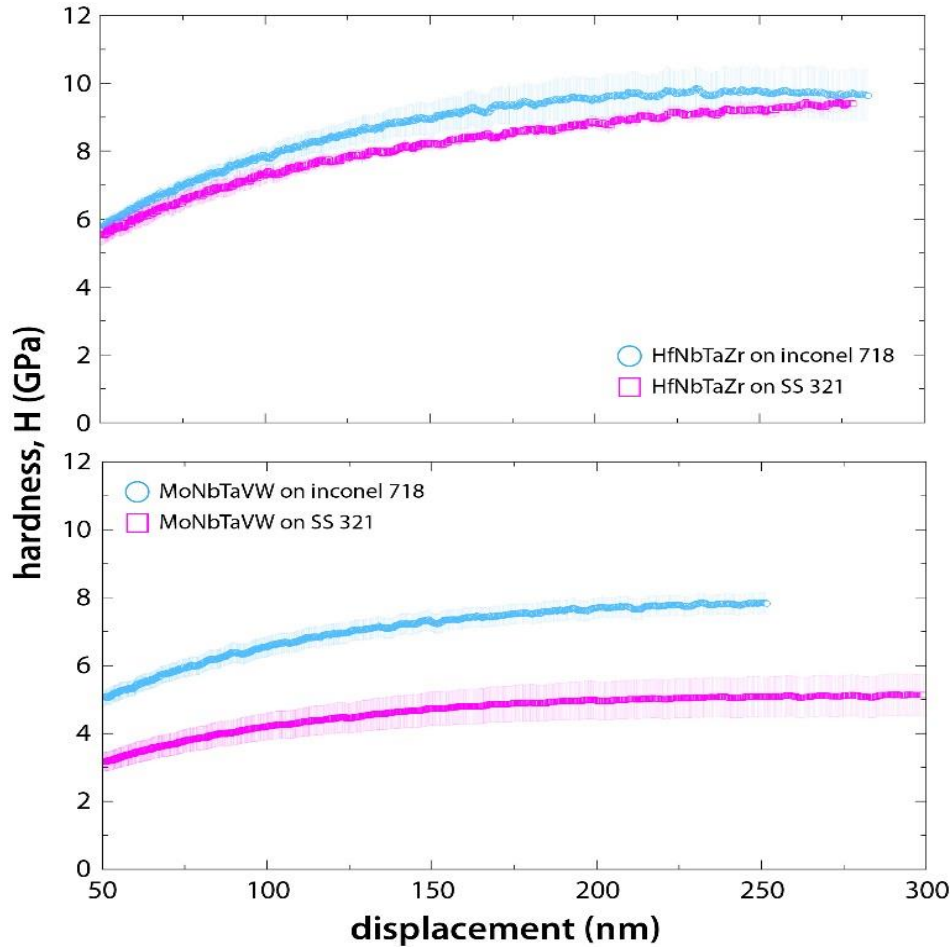

Figure 8. Nanoindentation hardness as a function of vertical displacement for four RHEA coatings.

Like microscratch testing, hardness values for nanoindentation were lower for both MoNbTaVW coatings. For MoNbTaVW Inconel 718 nanoindentation hardness was $H \cong 7.69\,\text{GPa}$ and had a storage modulus of $E' \cong 235\,\text{GPa}$. MoNbTaVW on SS 321 showed a hardness of $H \cong 5.08\,\text{GPa}$ and a storage modulus of $E' \cong 215\,\text{GPa}$. A recent investigation found the storage modulus ranging from $E' \cong 220 - 250\,\text{GPa}$ for MoNbTaVW thin films, which agrees with the values reported here [48]. Again, nanoindentation experiments yielded higher hardness values than microscratch experiments, for the same reasons hypothesized above. The substrate appeared to affect

nanoindentation hardness for MoNbTaVW ($\Delta H \cong 3$ GPa) more so than HfNbTaZr. Across all samples, RHEA coatings on Inconel 718 resulted in higher hardness than the corresponding coating composition on SS 321.

6 SUMMARY

A review of the literature indicates that the HfNbTaZr RHEA coating presented here is the first such manufactured based on the aforementioned, nearly-equiatomic elemental compositions, while the first MoNbTaVW coating was likely first manufactured in 2017 [14]. The APS and HVOF processes were used to apply the RHEA coatings onto SS 321 and Inconel 718 because these alloys are prevalent in industrial applications. HfNbTaZr was selected because it is suitable for harsh environments that do not include nuclear reactor radiation, while MoNbTaVW is suitable for harsh environments that include radiation.

Scratch and nanoindentation experiments were conducted to obtain experimental data for the friction coefficient as a function of applied force and position, as well as hardness as a function of strain rate. The HfNbTaZr and MoNbTaVW RHEA samples incurred low abrasive wear damage, as evidenced by wear coefficients in the range of $K \cong 10^{-4}$. Moreover, the HfNbTaZr wear coefficient ($K \cong 5 \times 10^{-4}$) was nearly two orders of magnitude lower than a similar RHEA, HfNbTiZr ($K \cong 10^{-2}$), suggesting that the substitution of Ti for Ta can increase wear resistance. The HfNbTaZr hardness ranged from 8.54 to 9.51 GPa, while that of MoNbTaVW ranged from 5.08 to 7.69 GPa; these compare favorably with similar RHEA coatings from the literature that ranged from 3.6 to 5.6 GPa.

The experimental data show excellent adhesive properties, high strength, reasonable homogeneity, and deposition characteristics. This research provides additional evidence that RHEA coatings can be suitable for harsh environment applications because of their resistance to abrasion, increased hardness, and high-entropy composition based on high-temperature refractory elements. The experimental data also indicate a strong potential for RHEA coatings to reduce erosion and provide high-temperature structural integrity in sCO2 Brayton Cycles, turbomachinery (e.g., diffusers and turbine blades), aerospace components (e.g., components based on Inconel 718), and advanced nuclear reactors.

REFERENCES

1. Senkov, O. N. et al., "Refractory High-Entropy Alloys", *Intermetallics*, Vol. 18, pp 1758-1765, DOI: 10.1016/j.intermet.2010.05.014, 2010.
2. Murty, B. S., J. W. Yeh, S. Ranganathan, and P. P. Bhattacharjee, *High-Entropy Alloys*, Elsevier, 2nd Ed., 2019.
3. Meghwal, A. et al., "Thermal Spray High-Entropy Alloy Coatings: A Review", *Journal of Thermal Spray Technology*, Vol. 29, pp 857-893, DOI: 10.1007/s11666-020-01047-0, 2020.
4. Rodriguez, S., *Applied Computational Fluid Dynamics and Turbulence Modeling: Practical Tools, Tips and Techniques*, Springer International Publishing, 1st Ed., ISBN 978-3-030-28690-3, DOI: 10.1007/978-3-030-28691-0, www.cfdturbulence.com, 2019.
5. UPT, United Protective Technologies, "Advanced Thin Film Coatings", www.upt-usa.com, 2019.
6. Ang, A. S. M. and C. C. Berndt, "A Review of Testing Methods for Thermal Spray Coatings", *International Materials Reviews*, Vol. 59, No. 4, pp 179-223, DOI: 10.1179/1743280414Y.0000000029, 2014.

7. "Technology Readiness Level Definition", NASA, https://www.nasa.gov/pdf/458490main_TRL_Definitions.pdf. Accessed on October 26, 2021.

8. Feng, X., J. U. Surjadi, and Y. Lu, "Annealing-Induced Abnormal Hardening in Nanocrystalline NbMoTaW High-Entropy Alloy Thin Films", *Materials Letters*, Vol. 275, DOI: 10.1016/j.matlet.2020.128097, 2020.

9. Rodriguez, S. et al., "Application of Refractory High-Entropy Alloys for Higher-Reliability and Higher-Efficiency Brayton Cycles and Advanced Nuclear Reactors", Sandia National Laboratories, SAND2021-11377, 2021.

10. Feng, X. B. et al., "Size Effects on the Mechanical Properties of Nanocrystalline NbMoTaW Refractory High Entropy Alloy Thin Films", *International Journal of Plasticity*, Vol. 95, pp 264-277, DOI: 10.1016/j.ijplas.2017.04.013, 2017.

11. Kim, H. et al., "Mechanical and Electrical Properties of NbMoTaW Refractory High-Entropy Alloy Thin Coatings", *International Journal of Refractory Metals & Hard Materials*, Vol. 80, pp 286-291, DOI: 10.1016/J.IJRMHM.2019.02.005, 2019.

12. Rodriguez, S., A. Kustas, and G. Monroe, "Metal Alloy and RHEA Additive Manufacturing for Nuclear Energy and Aerospace Applications", Sandia National Laboratories, SAND2020-7244, 2020.

13. Fleming, D. et al., "Corrosion and Erosion Behavior in Supercritical CO2 Power Cycles", *Proceedings of the ASME Turbo Expo 2014: Turbine Technical Conference and Exposition*, GT2014, Germany, DOI: 10.1115/GT2014-25136, 2014.

14. Poulia, A. et al., "Dry-Sliding Wear Response of MoTaWNbV High Entropy Alloy", *Advanced Engineering Materials*, Vol. 19, No. 2, DOI: 10.1002/adem.201600535, 2017.

15. Rodriguez, S., A. Kustas, and D. Ames, Non-Provisional Patent Application No. 17/062,136, "High Entropy Alloys, Refractory High Entropy Alloys, Methods of Selecting and Making, and Structures Formed from High Entropy and Refractory High Entropy Alloys", Sandia National Laboratories, 2020.

16. Baranova, A., "Russian Scientists Research Steel-Vanadium-Steel Laminate for Next-Gen Nuclear Reactors", ASM International, 2019.

17. Wright, R., "New Alloy Material Approved for Use in High-Temperature Nuclear Plants", Idaho National Laboratory, 2020.

18. Senkov, O. N. et al., "Development and Exploration of Refractory High-entropy Alloys—A Review", *J. Mater. Res.*, Vol. 1, 2018.

19. George, E. P., D. Raabe, and R. O. Ritchie, "High-Entropy Alloys", Nature Reviews Materials, Vol. 4, pp 515-534, 2019.

20. Wadsworth, J., T. G. Nieh, and J. J. Stephens, "Recent Advances in Aerospace Refractory Metal Alloys", *International Materials Reviews*, Vol. 33, No. 1, pp 131-150, DOI: 10.1179/imr.1988.33.1.131, 1988.

21. Corrosionpedia, "Refractory Metals: Properties, Types and Applications", https://www.corrosionpedia.com/2/1426/corrosion-101/refractory-metals-properties-types-and-applications. Accessed on June 4, 2021.

22. Mueller, F. et al., "On the Oxidation Mechanism of Refractory High-entropy Alloys", Corrosion Science, Vol. 159, 2019.

23. Jog, M. A. and L. Huang, "Transient Heating and Melting of Particles in Plasma Spray Coating Process", *Journal of Heat Transfer*, Vol. 118, pp 471-477, DOI: 10.1115/1.2825868, 1996.

24. Jacques, K., N. Murthy, S. Dixit, D. Berman, and S. Berkebile, "Method for Tribological Experiment to Study Scuffing Initiation on AISI 52100 Steel and Hard Ceramic Coatings, *Tribology International*, 107001, Vol. 160, 2021.

25. Tejero-Martin, D., M. R. Rad, A. McDonald, and T. Hussain, "Beyond Traditional Coatings: A Review on Thermal-Sprayed Functional and Smart Coatings", *Journal of Thermal Spray Technology*, Vol. 28, pp 598–644, DOI: 10.1007/s11666-019-00857-1, 2019.

26. Oksa, M. et al., "Optimization and Characterization of High Velocity Oxy-Fuel Sprayed Coatings: Techniques, Materials, and Applications", *Coatings*, Vol. 1, No. 1, pp 17-52, DOI: 10.3390/coatings1010017 2011.

27. Hodge, A. M. and T. G. Nieh, "Evaluating Abrasive Wear of Amorphous Alloys using Nanoscratch Technique", *Intermetallics*, Vol. 12, pp 741-748, DOI: 10.1016/j.intermet.2004.02.014, 2004.

28. Hutchings, I. and P. Shipway, *Tribology: Friction and Wear of Engineering Materials*, Butterworth-Heinemann, 2017.

29. Archard, J. F., "Contact and Rubbing of Flat Surfaces," *Journal of Applied Physics*, Vol. 24, p 981, DOI: 10.1063/1.1721448, 1953.

30. Ye, Y. X., C. Z. Liu, H. Wang, and T. G. Nieh, "Friction and Wear Behavior of a Single-Phase Equiatomic TiZrHfNb High-Entropy Alloy Studied Using a Nanoscratch Technique", *Acta Materialia,* Vol. 147*,* pp 78-89, DOI: 10.1016/j.actamat.2018.01.014, 2018.

31. Kato, K., "Abrasive Wear of Metals", *Tribology International*, Vol. 30, pp 333-338, DOI: 10.1016/S0301-679X(96)00063-1, 1997.

32. Hua, N. et al., "Mechanical, Corrosion, and Wear Properties of Biomedical Ti-Zr-Nb-Ta-Mo High Entropy Alloys", *Journal of Alloys and Compounds*, Vol. 861, 157997, DOI: 10.1016/j.jallcom.2020.157997, 2021.

33. Nyakiti, L. O. and A. F. Jankowski, "Characterization of Strain-Rate Sensitivity and Grain Boundary Structure in Nanocrystalline Gold-Copper Alloys", *Metallurgical and Material Transactions A*, Vol. 41, pp 838-847, DOI: 10.1007/s11661-009-9996-9, 2010.

34. Schuh, C. A., T. G. Nieh, and T. Yamasaki, "Hall-Petch Breakdown Manifested in Abrasive Wear Resistance of Nanocrystalline Nickel", *Scripta Materialia*, Vol. 46, pp 735-740, DOI: 10.1016/S1359-6462(02)00062-3, 2002.

35. Melia, M. A. et al., "High-Throughput Additive Manufacturing and Characterization of Refractory High Entropy Alloys", *Applied Materials Today*, Vol. 19, 100560, DOI: 10.1016/j.apmt.2020.100560, 2020.

36. Maiti, S. and W. Steurer, "Structural-Disorder and Its Effect on Mechanical Properties in Single-Phase TaNbHfZr High-Entropy Alloy", *Acta Materialia*, Vol. 106, pp 87-97, DOI: 10.1016/j.actamat.2016.01.018, 2016.

37. Srikanth, M. et al., "A Review of the Latest Developments in the Field of Refractory High-Entropy Alloys", *Crystals*, Vol. 11, 612, DOI: 10.3390/cryst11060612, 2021.

38. Senkov, O. N. et al., "Mechanical Properties of $Nb_{25}Mo_{25}Ta_{25}W_{25}$ and $V_{20}Nb_{20}Mo_{20}Ta_{20}W_{20}$ Refractory High Entropy Alloys", *Intermetallics*, Vol. 19, pp 698-706, DOI: 10.1016/j.intermet.2011.01.004, 2011.

39. Sadeghilaridjani, M. et al., "Strain Rate Sensitivity of a Novel Refractory High Entropy Alloy: Intrinsic Versus Extrinsic Effects", *Materials Science and Engineering: A*, Vol. 766, 138326, DOI: 10.1016/j.msea.2019.138326, 2019.

40. Xiao, Y. et al., "Micro-Compression Studies of Face-Centered Cubic and Body-Centered Cubic High-Entropy Alloys: Size-Dependent Strength, Strain Rate Sensitivity, and Activation Volumes", *Materials Science and Engineering: A*, Vol. 790, 139429, DOI: 10.1016/j.msea.2020.139429, 2020.

41. Sadeghilaridjani, M. et al., "Deformation and Tribological Behavior of Ductile Refractory High-Entropy Alloys", *Wear*, Vols. 478-479, 203916, DOI: 10.1016/j.wear.2021.203916, 2021.

42. Wei, Q. et al., "Effect of Nanocrystalline and Ultrafine Grain Sizes on the Strain Rate Sensitivity and Activation Volume: FCC Versus BCC Metals", *Materials Science and Engineering: A*, Vol. 381, pp 71-79, DOI: 10.1016/j.msea.2004.03.064, 2004.

43. Fitzgerald, S. P., "Kink Pair Production and Dislocation Motion", *Scientific Reports*, Vol. 6, 39708, DOI: 10.1038/srep39708, 2016.

44. Oliver, W. C. and G. M. Pharr, "An Improved Technique for Determining Hardness and Elastic Modulus Using Load and Displacement Sensing Indentation Experiments", J. Mater. Res., Vol. 7, No 6, pp 1564-1583, 1992.

45. Phani, P. S. and W. C. Oliver, "A Critical Assessment of the Effect of Indentation Spacing on the Measurement of Hardness and Modulus Using Instrumented Indentation Testing", Materials and Design, Vol. 164, doi.org/10.1016/j.matdes.2018.107563, 2019.

46. Nix, W. D. and H. Gao, "Indentation Size Effects in Crystalline Materials: A Law for Strain Gradient Plasticity", *Journal of the Mechanics and Physics of Solids*, Vol. 46, pp 411-425, DOI: 10.1016/S0022-5096(97)00086-0, 1998.

47. Gorsse, S. et al., "Database on the Mechanical Properties of High Entropy Alloys and Complex Concentrated Alloys", *Data in Brief*, Vol. 21, pp 2664-2678, DOI: 10.1016/j.dib.2018.11.111, 2018.

48. Xia, A. et al., "Angular-Dependent Deposition of MoNbTaVW HEA Thin Films by Three Different Physical Vapor Deposition Methods", *Surface and Coatings Technology*, Vol. 385, 125356, DOI: 10.1016/j.surfcoat.2020.125356, 2020.

ACKNOWLEDGMENTS